Land Cover Classification and Change Analysis in the Horqin Sandy Land From 1975 to 2007

Hasi Bagan, Wataru Takeuchi, Tsuguki Kinoshita, Yuhai Bao, and Yoshiki Yamagata

Abstract—Observations over the last three decades show that desertification poses a serious threat to the livelihood and productivity of inhabitants of the Horqin Sandy Land region of China. We evaluated the dynamics and trends of changes of land cover in the Horqin Sandy Land by using Landsat archive images from 1975, 1987, 1999, and 2007. We applied two supervised classification methods, the self-organizing map neural network method and the subspace method. Our analyses revealed significant changes to land cover over the period 1975–2007. The area of cropland doubled over the last three decades. This expansion was accompanied by large increases in water consumption and considerable loss of areas of grassland and woodland. Many lakes and rivers shrank rapidly or disappeared in this region between 1975 and 2007. The sandy area expanded rapidly from 1975 to 1987 but gradually slowed thereafter.

Index Terms—Change detection, desertification, Horqin Sandy land, land cover, landsat.

I. INTRODUCTION

THE Horqin Sandy Land is in the arid and semi-arid southeastern part of the Inner Mongolian Autonomous Region in China. This region has undergone severe desertification in recent decades [1], [2]. Increasing amounts of airborne dust and frequent sandstorms caused by desertification have severely affected the populations and productivity of major Chinese cities. During the last three decades, both the frequency and intensity of dust and sandstorms have increased, their geographic coverage has expanded, and the amount of damage they cause has grown; they affect not only major Chinese cities but also areas of Japan and Korea [3].

Numerous scientists have suggested that desertification in the Horqin Sandy Land has been caused primarily by human activities. Population increases, excessive land development, overgrazing, and collection of fuel wood have had key roles in this

desertification process [1], [4], [5]. Since the 1970s, immigration of people [6] has rapidly increased the human population of grassland areas in the Horqin region. Environmental changes have led to the traditional nomadic lifestyle of the local people being gradually replaced by modern settlements. Consequently, the number of grazing animals and the land area developed for both agricultural and urban use has increased [5]–[7].

Agricultural expansion and overgrazing became a serious problem in the early 1980s as a result of a government rural reform program in this region [7], [8]. Furthermore, a market economy was introduced to Inner Mongolia in the mid-1980s, and this included a system that allocated responsibility for livestock, cropland, and usable grassland to households [9]. The household responsibility system stimulated a rapid increase in both the area of cropland and the number of livestock in the Horqin Sandy Land. These essentially uncontrolled activities caused destruction of woodland and grassland, degradation of soil, and increased water consumption [10], [11].

In 2001, a series of large sandstorms swept through much of northern China [12]. These storms alerted the Chinese government to the urgent need for a sustainable land-use policy for the Horqin Sandy Land, a region of sandy soils and sparse vegetation cover that provides a sediment substrate source for such storms.

The government initiated several projects to reduce the effects of dust and sandstorms in the region. Through these projects, the families of local herders and farmers were moved from desertified steppe and ecologically fragile farmland and settled in new towns.

Agricultural expansion and urbanization in this region led to dramatic changes in land use. In eastern Inner Mongolia between 1986 and 1996, grassland conversion produced one million hectares of new farmland, matching the amount of farmland created during the Cultural Revolution (1966–1976) [13]. Expanding cropland areas and urbanization greatly increase water and chemical fertilizer use and considerably reduce biodiversity through the loss, modification, and fragmentation of habitats [14].

Remotely sensed data collected over a span of years can be used to identify and characterize both natural and anthropogenic changes over large areas of land [15], [16]. Landsat satellite images are ideal for this purpose; imagery recorded over nearly four decades provides a unique resource for temporal analysis of land cover [17].

The purpose of this study was to investigate spatial and temporal land-cover changes in the Horqin Sandy Land and to investigate the possible causes of those changes. To do this, we applied land-cover classification schemes to Multispectral
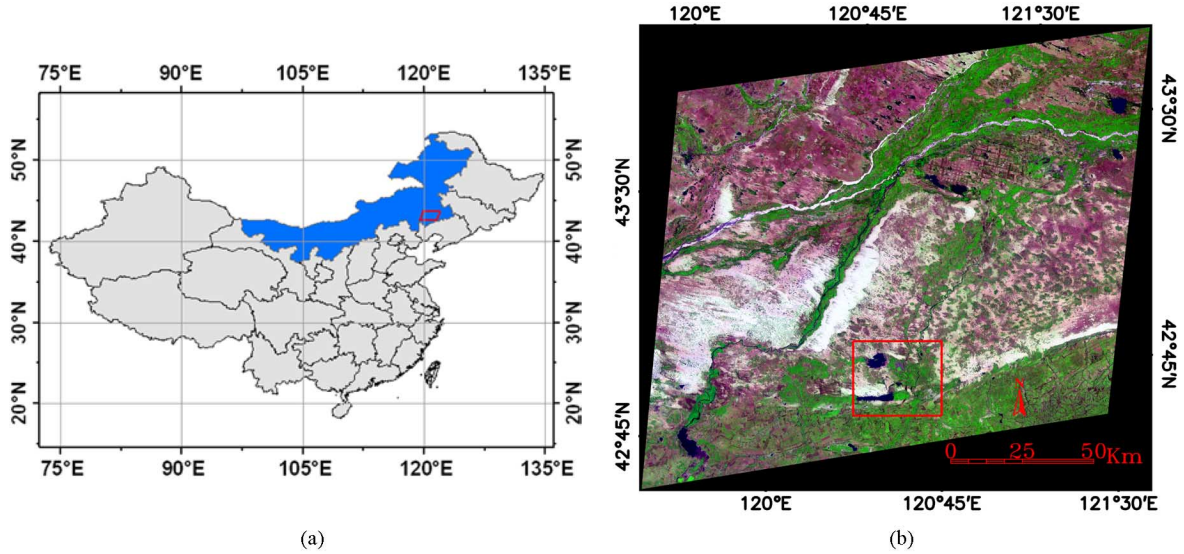
Fig. 1. Location of the study area (red rectangle in left-hand panel). The right-hand panel shows the September 1999 full-scene Landsat TM image (RGB = bands 5, 4, 3) of the study area. The red rectangle in the right-hand panel indicates the area of the images shown in Fig. 4.

TABLE I
SUMMARY OF LANDSAT TIME-SERIES SCENES USED IN THIS STUDY

Sensor	Data acquired	Path /row	Path / row center	Spatial resolution	Classification method
Landsat-2 MSS	1975-09-06	130/30	43.073N, 121.274E	60 M	SOM
Landsat-2 MSS	1976-07-27	131/30	43.108N, 119.701E	60 M	SOM
Landsat-5 TM	1987-08-11	121/30	43.166N, 120.819E	30 M	Subspace
Landsat-7 ETM+	1999-09-05	121/30	43.191N, 120.708E	30 M	Subspace
Landsat-5 TM	2007-09-03	121/30	43.175N, 120.752E	30 M	Subspace

Scanner (MSS), Thematic Mapper (TM), and Enhanced Thematic Mapper Plus (ETM+) sensor images recorded between 1975 and 2007, which we acquired from the Landsat archive.

We used two supervised classification methods, the self-organizing map (SOM) neural network method and the subspace method, to accurately classify land cover on Landsat images recorded in 1975, 1987, 1999, and 2007. This allowed us to quantitatively present land-cover changes between 1975 and 2007, report on the trends of those changes, and discuss some of the most likely causes of desertification in the Horqin Sandy Land.

II. METHODOLOGY

A. Study Area

The Horqin Sandy Land is in the southeastern part of the Inner Mongolia Autonomous Region of China ($119°21'$–$122°14'$E, $42°14'$–$44°7'$N; Fig. 1) and covers an area of about 30,000 km^2. It has a continental arid and semi-arid climate with an annual mean temperature of about 6.8 °C, mean annual precipitation of 366 mm, and annual mean potential evaporation of 1935 mm. The annual frost-free period is about 130–150 days [18].

B. Data Description

We acquired five Landsat images to achieve multitemporal coverage of the area and thus detect temporal changes of land cover. Table I provides information on the image data and classification methods used. The images were geometrically rectified to an Albers equal-area projection system by using a different number (21–28) of ground control points (GCPs) for each image. GCPs were well dispersed throughout each scene and yielded root-mean-square errors of less than 0.65 pixels. The spatial resolution of TM and ETM+ data was 30 m for bands 1–5 and 7. Where TM band 6 and ETM+ band 61 (thermal infrared) were acquired at 120 m resolution, they were resampled to 30 m using the cubic convolution method done by U.S. Geological Survey. The spatial resolution of the four MSS bands was approximately 79 m, but these data were resampled to 60 m done by U.S. Geological Survey.

The 1975 MSS data do not cover a very small area at the right-hand edge (about 10%) of the study area, so we used a mosaic of 1975 and 1976 MSS images to attain full area coverage. For this mosaic, the 1975 MSS data were used as the base image and the 1976 MSS data were color balanced to match the 1975 data range (hereafter we refer to this mosaic as the 1975 MSS data).

In addition to above Landsat data, ancillary GIS datasets and other ancillary satellite data were also used as reference data to assist in our field investigations (Table II). The GIS data include, the National Land-Use/Land-Cover data sets (NLCD, hereafter) of the year 1995 and 2000 at a spatial scale of 1:100000 [19], LREIS digital maps at the scale of 1:4000000 [20]. The vege-

TABLE II
ANCILLARY DATA SETS USED FOR SUPPORT GROUND REFERENCE DATA COLLECTION

Ground reference data	Ancillary data sets
1. 1975 MSS	Landsat MSS scenes (16 May 1976, 27 July 1976, and 8 August 1977), and LREIS maps (1996)
2. 1987 TM	Landsat TM (23 September1988 and 20 June 1989), LREIS maps (1996), and NLCD of the year 1995
3. 1999 ETM+	Landsat ETM+ (11 August 1999), Landsat TM (03 June 2000) , and NLCD of the year 2000
4. 2007 TM	SPOT-5 (2005-2006), Landsat TM (30 May 2007), and ALOS PRISM and AVNIR-2 (07 October 2007)

TABLE III
DESCRIPTION OF LAND-COVER CLASSES AND PIXEL COUNTS BY LAND-COVER CLASS

Land cover class	Class description	1975 MSS		1987 TM		1999 ETM		2007 TM	
		Study	Test	Study	Test	Study	Test	Study	Test
1. Water	Water bodies	521	420	380	277	256	241	211	224
2. Woodland	Forests with canopies greater than 50%	443	370	646	423	417	341	401	341
3. Cropland	Irrigated or nonirrigated cultivated lands for crops	873	604	1325	986	944	751	958	751
4. Sand	Sand dune and sandy land covered with less than 5% vegetative cover	344	305	306	258	393	376	393	450
5. Sparse grass	Grassland, occasional tree and shrub with canopies greater than 5% total vegetative cover and less than 50% vegetative cover	632	542	418	338	517	417	572	435
6. Grassland	Dominated by grasslands and shrubs with canopies greater than 50%	1275	874	745	503	739	479	673	399
7. Urban/Built-up	Buildings, concrete, asphalt paved road, and other human-made structures	155	109	251	226	427	384	427	422
8. Bare	Salinization soils, bare ground and exposed soil with less than 5% total vegetative cover	240	194	352	260	388	335	411	311
9. Wetland	Mixture of water and herbaceous or woody vegetation, floodlands	485	358	362	268	247	204	234	160
Total		4968	3776	4785	3539	4328	3528	4280	3493

tation map (published in 1979), soil map (published in 1978), desert map (published in 1988), road map (published in 1988), and river map (published in 1989) in the LREIS digital maps were used. The ancillary satellite data used in this study was: a mosaic of SPOT-5 images (2.5-m spatial resolution) acquired during 2005–2006; an ALOS bundle comprising a panchromatic PRISM image (2.5-m spatial resolution) and multispectral spatial resolution AVNIR-2 images (10-m spatial resolution; three visible bands and one near-infrared band) acquired on October 7, 2007; three Landsat MSS scenes (acquired on 16 May 1976, 27 July 1976, and 8 August 1977); four Landsat TM scenes (acquired on 23 September 1988, 20 June 1989, 03 June 2000, and 30 May 2007); and a Landsat ETM+ (acquired on 11 August 1999). As well, other ancillary data such as Shuttle Radar Topography Mission (SRTM) elevation data [21] was used to provide information about elevation of the area and to help locate the ground reference site.

To thoroughly understand the ground truth situation, six field surveys were conducted in 2000, 2002, 2003, 2006, 2007, and 2009 at a number of locations across the study area. During the field surveys, photos were taken for ground reference data with GPS facilities and interviews with local inhabitants were recorded.

Nine land-cover types were defined based on our field investigations (Table III). The ground reference sample sites were obtained from extensive field survey. Ground reference data sites were selected for each mapping class for each Landsat recording date to accurately portray the spectral complexity and variability within each class. All initial digitized ground reference sites (polygons) were compared with the corresponding Landsat imagery acquired in 1975, 1987, 1999, and 2007, respectively, to

provide the correct interpretation at the time of the image date. In addition, other ancillary satellite images and ancillary GIS datasets (Table II) were used to support image interpretation and to provide as much information as possible to help to locate the ground reference site. When the sample site (polygon) contained multiple classes or was poorly delineated, a new homogeneous sample polygon (or line) was delineated within the original site (polygon). A subset of the image interpreted sites was also field visited and additional sites were collected. The finally selected reference sites were either polygonal or linear, and their locations were recorded using the ITT ENVI software package. The reference sites were then divided into training and testing sets to ensure spatial disjointing and to reduce the potential for correlation between the study data and the test data (Table III).

III. CLASSIFICATION METHODS

In recent years, many advanced methods have been applied in Landsat image classification, each of which has both strengths and limitations. We examined two classification methods, the SOM and subspace methods, for each of the Landsat data sets. Our testing showed that for MSS data classification, the SOM method provides better classification accuracy than the subspace method. However, for TM and ETM+ data, the subspace method results are better than those of the SOM method. Thus, the SOM method was chosen for 1975 MSS classification, and subspace method was chosen for TM and ETM+ data classification. The following two subsections present descriptions of the SOM and subspace classification methods.
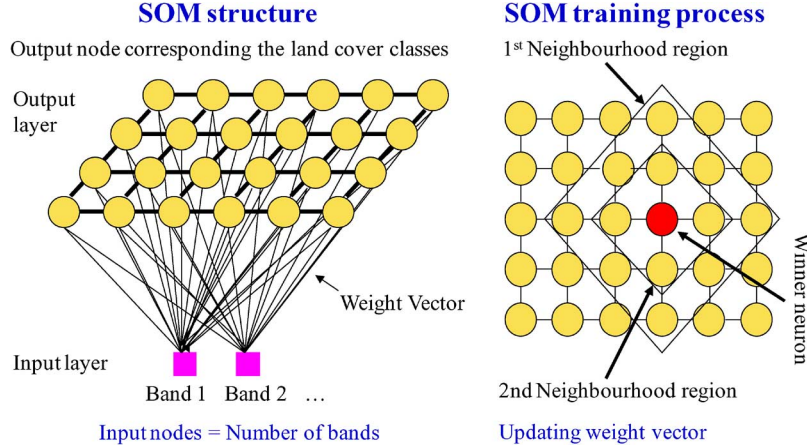
SOM structure

Output node corresponding the land cover classes

SOM training process

1st Neighbourhood region

Winner neuron

Output layer

Weight Vector

Input layer

Band 1   Band 2   …

Input nodes = Number of bands

2nd Neighbourhood region

Updating weight vector

Fig. 2.   SOM structure and training process.

A. SOM

There are many neural network methods available for image classification. Among these, the SOM method is more successful in classification and pattern recognition [22]. The SOM method generally uses two layers, an input layer and an output layer. The input layer nodes are all connected to those of the output layer (competitive layer).

In SOM, both the distribution and the topology of features of the input layer are identified by using an unsupervised, competitive, neighborhood learning method. The high-dimensional data are then projected onto a low-dimensional map (competitive layer), usually as a two-dimensional map. The neurons (nodes) in the competitive layer are arranged by topological order in the input space [23], [24].

The SOM computes the Euclidean distance of the input vector (pixel) x to each neuron, and find the winning neuron using the nearest-neighbor rule. Then SOM applies an iterative procedure to update the winning neuron's weight vector in the competitive layer. However, instead of updating only the winning neuron's weight vector, all neurons within a defined neighborhood of the winning neuron are updated by a self-organization process (Fig. 2).

After a winning neuron has been identified, it and its neighbors are updated to reduce the difference between the winning neuron and the input vector. The weight vector m_i updating rule for a neighborhood neuron r_i is given by

$$m_i(t+1) = m_i(t) + \alpha(t)h_{ci}(t)[x - m_i(t)] \qquad (1)$$

where $0 < \alpha(t) < 1$ is the learning-rate function, and h_{ci} is the neighborhood function. Both $\alpha(t)$ and the width of h_{ci} decrease gradually with increasing step t.

Selecting a neighborhood kernel function is important for SOM land-cover classification. Instead of simple neighborhood function [25], we adopt the Gaussian kernel as the neighborhood function. The Gaussian neighborhood function we used was

$$h_{ci}(t) = \exp\left[-\frac{\|r_c - r_i\|^2}{2\sigma^2(t)}\right] \qquad (2)$$

where r_c is the winning neuron, r_i is the activated neuron in the neighborhood region, and $\sigma(t)$ is a neighborhood width parameter that may or may not be time variant. We defined $\sigma(t)$ as

$$\sigma(t) = R(t) \qquad (3)$$

where $R(t)$ is the neighborhood radius at iteration step t. The neighborhood radius $R(t)$ is decreased until it reaches the predefined final radius value according to

$$R(t) = R(0) - [A \times (t + A \times t)] \qquad (4)$$

where $A = R(0)/T$, T is the maximum iteration time, $R(0)$ is the initial neighborhood radius, and $[v]$ denotes the maximum integer that does not exceed v.

After SOM training, supervised learning vector quantization (LVQ) was implemented to fine tune the SOM's weighting vectors [25]. The supervised LVQ employs the same network architecture as the SOM. The LVQ is based on the known classification of feature vectors, and can be treated as a supervised version of the SOM. Assuming that the pixel x is presented at training time t, weight vector m_c of neuron c is updated as

$$m_c(t+1) = m_c(t) + \eta(t)[x - m_c(t)]$$
$$\text{if } x \text{ and neuron } c \text{ belong to the same class}$$
$$m_c(t+1) = m_c(t) - \eta(t)[x - m_c(t)]$$
$$\text{if } x \text{ and neuron } c \text{ belong to different classes}$$
$$m_i(t+1) = m_i(t) \text{ for } i \neq c. \qquad (5)$$

where $0 < \eta(t) < 1$ is the learning-rate function and starts with a small $\eta(0)$, usually less than 0.1.

To verify the performance of the above SOM method, we performed simulations on the 1975 MSS data set. The simulation results showed that the above SOM method provided classification accuracy of 71%, which was 3.3% better than that produced by SOM based on the simple neighborhood function. We found that the optimal parameters for SOM learning were as follows: a two-dimensional competitive layer of 11×11 (121) nodes; learning rate $\alpha(t)$ gradually converging from 0.9 to 0.0015 as learning progresses; and neighborhood learning area converging from 7×7 nodes to a single node as learning

progresses. The maximum number of SOM iterations was set at 3000. The parameters for LVQ learning were a maximum number of iterations of 1000 and a learning rate $\eta(t)$ gradually converged from 0.003 to 0.00001.

B. Subspace Method

The subspace method [26] has been widely used for pattern recognition and has recently been applied to classification of remote sensing data [27].

Like SOM, the subspace method projects high-dimensional input data onto a low-dimensional feature space, but it differs from SOM in that the different classes are represented in their own low-dimensional subspaces.

The basic subspace method is called class-featuring information compression (CLAFIC) [28], which is achieved as follows. Let N be the number of input feature dimensions, which, in our case, is equal to the number of Landsat bands; let $\varphi_{k,i} (1 \leq i \leq r, 1 \leq k \leq K)$ be the basis vectors of the subspace of class C^k, which are computed from training set of the class by the principal component analysis; here, r is the subspace dimension and K is the number of classes. The calculation of the square of the projection length P_k of pixel x in the subspace of class C^k is given by

$$P_k = \sum_{i=1}^{r} (x, \varphi_{k,i})^2 / \|x\|^2. \tag{6}$$

After computing the projection lengths between pixel x and each subspace, pixel x is placed in the class that has the largest projection length.

Misclassifications in CLAFIC are caused mainly by overlap of class subspaces. Averaged learning subspace method (ALSM) has been proposed as a way to separate subspaces [26], [29]. In ALSM, class subspaces are slowly rotated to reduce the overlap between them. ALSM is described as follows. At iteration k, the conditional correlation matrix is computed from

$$P_k^{(i,j)} = \sum_{x} \{xx^T | x \in C^i, x \mapsto C^j\}; \tag{7}$$

here, the symbol $\mapsto$ indicates that the pixel x of class C^i has been misclassified into class C^j.

After the conditional correlation matrix has been generated, the correlation matrix for class C^i is updated as follows:

$$P_k^{(i)} = P_{k-1}^{(i)} + \alpha \sum_{j=1, j \neq i}^{K} P_k^{(i,j)} - \beta \sum_{j=1, j \neq i}^{K} P_k^{(j,i)} \tag{8}$$

where α and β are learning parameters; both usually have small, constant positive values. Then, the eigenvalues and eigenvectors of $P_k^{(i)}$ can be calculated to generate a new subspace of class C^i. This iterative process ends when either the entire training data are fully recognized or the maximum number of iterations has been reached. Selection of both the subspace dimension parameters and learning parameters is important in the subspace training phase. If in ALSM the subspace dimensions for each class are the same and the two learning parameters are equal, the accuracy of recognition is optimized [30]. In this study, the subspace dimension is fixed at 3 for 1987 TM, 1999 ETM+, and

2007 TM; the optimal learning parameters (α and β) are fixed at 0.26 for 1987 TM, 0.26 for 1999 ETM+, and 0.07 for 2007 TM; and the number of optimal training iterations are 56 for 1987 TM, 95 for 1999 ETM+, and 72 for 2007 TM.

IV. RESULTS AND DISCUSSION

We wrote programs for the SOM and subspace methods in C/C++ programming language (Microsoft Visual Studio 2005), which allowed us to apply the classification methods discussed above to our data. The MSS image was classified as 60-m resolution and the TM and ETM+ images as 30-m resolution.

The confusion matrix (error matrix) is a commonly used tool for assessment of accuracy of land-cover classification [31]. The producer's and user's accuracies are ways of representing individual category accuracies instead of just the overall classification accuracy. Let $[p_{ij}]_{n \times n}$ is a confusion matrix, p_{ij} is the number of pixels in mapped land cover class i and reference land cover j; $p_{i+} = \sum_{j=1}^{n} p_{ij}$ is the number of pixels in mapped land cover class i; and $p_{+j} = \sum_{i=1}^{n} p_{ij}$ is the true number of pixels in land cover class j. The user's accuracy for land-cover class i is defined as

$$P_{UAi} = \frac{p_{ii}}{p_{i+}}. \tag{9}$$

The producer's accuracy for land-cover class j is defined as

$$P_{PAj} = \frac{p_{jj}}{p_{+j}}. \tag{10}$$

Confusion matrices comparing test (reference) data to classification results were created, and overall accuracy, producer's and user's accuracies, and κ statistics of agreement were generated (Table IV). Overall accuracies were greater than 86% for the TM and ETM+ images, and the corresponding κ statistics were greater than 0.84. In comparison, the MSS image showed an overall classification accuracy of 70.66%, with a κ statistic of 0.66, both lower than those of the TM and ETM+ images.

The four vegetation types (woodland, cropland, sparse grass, and grasslands) were generally classified well in TM and ETM+ data, with producer accuracies greater than 78%, except for grassland in the 2007 data. The accuracy of classification of vegetation classes for MSS data was more variable, but we considered these data to be moderately well to well classified. The urban/built-up class was well classified in TM and ETM+ data, with producer accuracies greater than 88%, but posed problems for the MSS data where it was confused with both grassland and water. Wetland was the most difficult of all categories to classify and was confused with woodland and cropland for all data sets.

Full-scene land-cover classification maps for each of the four years are shown in Fig. 3, and detailed land-cover maps for the area around Daqintala town are shown in Fig. 4 (see Fig. 1 for location of the detailed maps). Both sets of land-cover maps show that over the last three decades there has been a vast expansion of cropland along rivers and around lakes as well as a general expansion to the southern and northeastern parts of the study area. The two time series of maps clearly show serious losses of areas of woodland, grassland, and water. The largest areas of sand have developed in the western part of the study area,

TABLE IV
ACCURACY OF CLASSIFICATIONS FOR THE FOUR LANDSAT-DERIVED LAND-COVER MAPS, SHOWN AS PRODUCER'S AND USER'S ACCURACIES
FOR EACH CLASS, OVERALL ACCURACY, AND κ STATISTICS

Land Cover Class	1975 MSS		1987 TM		1999 ETM+		2007 TM	
	Prod.	User	Prod.	User	Prod.	User	Prod.	User
1. Water	95.48	87.36	95.31	98.14	94.19	96.60	92.41	97.18
2. Woodland	53.51	53.37	85.11	89.55	88.56	90.69	96.19	93.71
3. Cropland	50.33	53.52	93.1	89.65	93.08	90.19	83.62	82.52
4. Sand	92.13	98.25	100	100	92.29	90.13	92.44	100
5. Sparse grass	82.47	80.11	85.5	80.28	78.18	86.02	87.13	82.75
6. Grasslands	56.52	65.95	93.44	83.63	85.8	78.29	71.43	67.86
7. Urban/Built-up	43.12	64.38	91.59	92.41	88.8	94.46	95.73	96.19
8. Bare	91.24	79.02	92.69	94.88	86.27	90.31	95.18	96.42
9. Wetland	89.11	65.37	63.43	91.40	81.37	77.21	56.25	60.81
Overall accuracy	70.66		89.77		88.1		86.83	
κ coefficient	0.66		0.8795		0.8634		0.8486	

Notes: Prod. indicates the Producer's accuracy and User indicates the User's accuracy.

(a) 1975 MSS

(b) 1987 TM

(c) 1999 ETM+

(d) 2007 TM

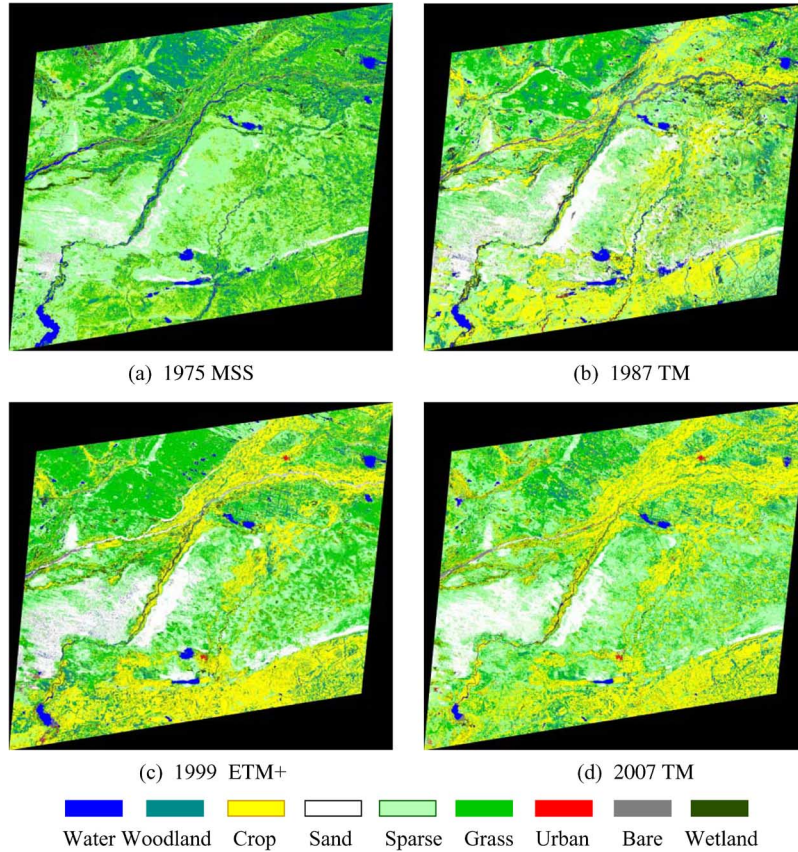Water Woodland Crop Sand Sparse Grass Urban Bare Wetland

Fig. 3. Time series of land-cover maps of the study area in (a) 1975, (b) 1987, (c) 1999, and (d) 2007.

and areas of bare ground have appeared mainly along rivers and around lakes.

There are several major trends evident in the changes of land cover and they are consistent over the period 1975–2007 (Figs. 3, 4, and 5). The area of water bodies decreased as did areas of woodland and grassland, and there was a marked increase in areas of cropland. Previous studies [32] also reported that grassland transformed into cropland at the village scale in Horqin sandy land.

The area of cropland doubled over the past three decades, increasing from 15.8% of the study area in 1975 to 31.7% in 2007. In contrast, the area of water bodies decreased from 2.1% in 1975 to 0.6% in 2007, while the areas of woodland and grassland decreased from 13.1% and 28.5%, respectively, in 1975, to 5.8% and 19.7%, respectively, in 2007. However, from 1987 to 2007, the area of the woodland stopped the tendency to decrease.
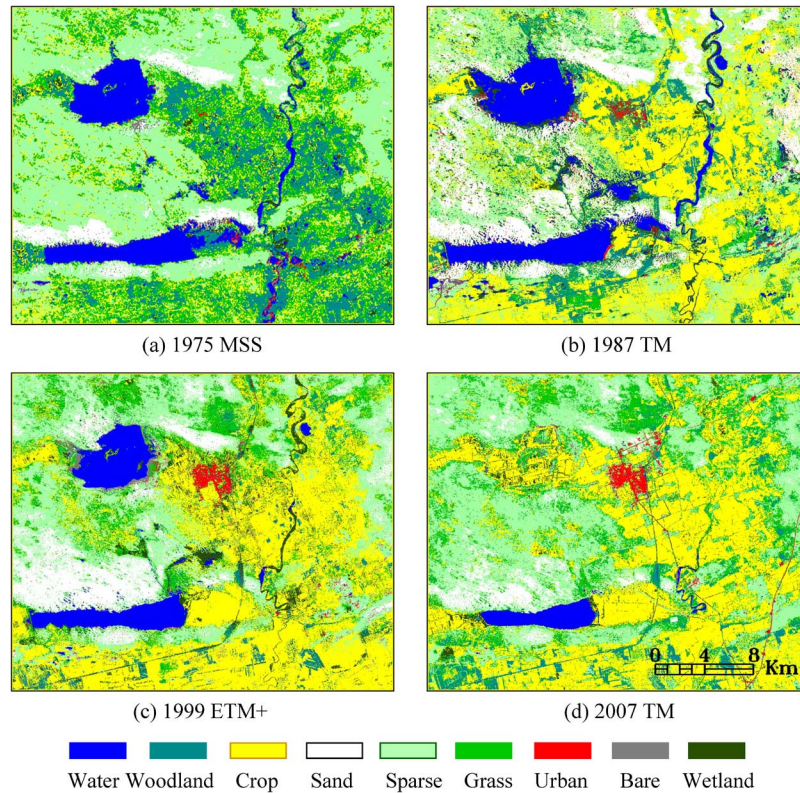
Fig. 4. Time series of detailed land-cover classification maps around Daqintala town in Inner Mongolia for (a) 1975, (b) 1987, (c) 1999, and (d) 2007. The location of the maps is shown in Fig. 1.

For the sandy land, the most rapid desertification occurred between 1975 and 1987. Over this period, the sand area increased from 4.1% to its maximum of 11.5% in 1987. Land rehabilitation after 1987 resulted in a steady decrease of sand area to 7.8% in 2007.

For the total area of grassland area and sparse-grass, the most rapid decrease occurred between 1975 and 1987. Over this period, the total area of grassland and sparse-grass decreased from 60.65% to 44.44%. However, after 1987 there was a steady increase of total area of grass land and sparse-grass to 50.45% in 2007. In reaction to land degradation events, the central government initiated the Sloping Land Conversion Program (also known as Grain for Green) in 1999, with particular emphasis on west China. This policy has been introduced in different ways in Inner Mongolia. Xun and Bao [33] reported that the ecological reconstruction policy in Inner Mongolia is implementation of the ecological migration policy. Under the new policy, all of the areas affected by serious ecological degradation are sealed off for more than five years and no grazing will be allowed in these areas. Our result shows that the policy shift successfully suppressed the sand area in Horqin sandy land.

In addition to the major conversion of areas of woodland, grassland, and water to cropland, other changes of land-cover are evident. These include transitions of sparse grass to sand, woodland and grassland converted to urban areas, and reversals of these changes in some instances (Figs. 3 and 4).

We considered in detail the changes to areas of cropland and water between 1987 and 2007 (Fig. 6). During this interval, areas of cropland expanded mainly along river courses and showed some contraction in sandy regions. These changes were the result of two government initiatives: the Sandstorm Source Control project and the Ecological Migration project. Through these projects, the families of local herders and farmers were moved from desertified steppe and ecologically fragile farmland and settled in new villages which mainly located along river courses. Over the period from 1987 to 2007, these government policies led to a reduction in the total area of sand dunes but also led to an increase in cropland, mainly in lowland areas and near river banks.

Croplands were developed and later abandoned on some sandy areas during the period from 1987 to 2007 [Fig. 6(a)]. The main reason for their abandonment was the sandy areas supported a decreasing yield, which was quickly overtaken by sand. In areas of increased cropland, rapid shrinkage and disappearance of water-covered areas occurred [Fig. 6(b)]. During this period, newly opened croplands were distributed along river banks and in grassland areas and areas of sand dunes were transformed for small-scale cultivation.

Large areas of irrigated cropland expanded rapidly along river banks, and even larger areas of irrigated croplands were developed on river plains where there was access to surface water or ground water. Consequently, water consumption increased as the cropland area expanded, thus decreasing the water-covered area by a factor of around three (from 1.9% in 1987 to 0.6% in 2007). Previous studies have indicated that the major cause of desertification of the Horqin Sandy Land is a decrease in ground
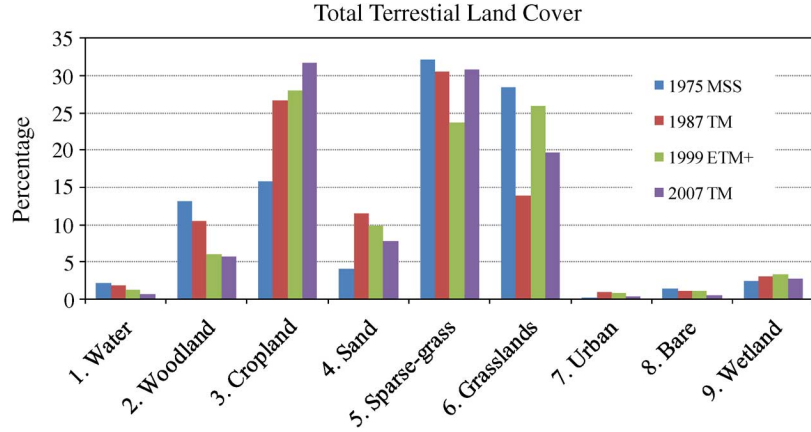
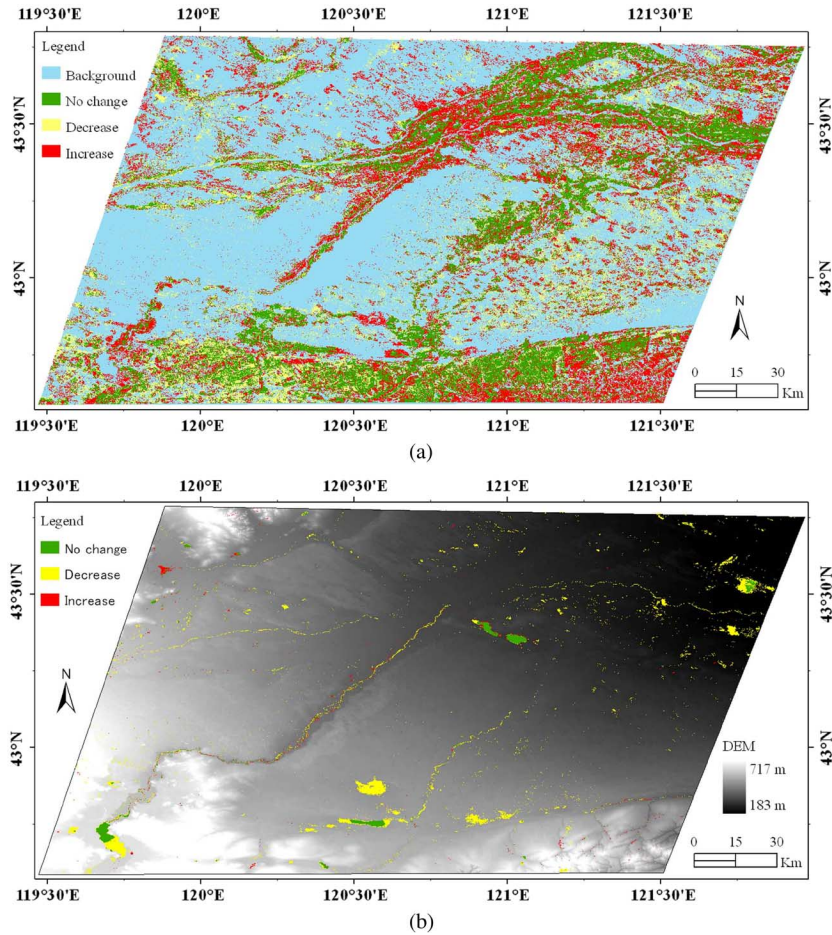Fig. 5.   Percentage of the study area covered by each land-cover class in 1975, 1987, 1999, and 2007.

Fig. 6.   Changes to the areas of (a) cropland and (b) water between 1987 and 2007. The gray image of panel (b) is a DEM generated from SRTM data.

water levels because of development of croplands on the alluvial and flood plains at the margins of desert areas [34].

Changes to land cover also caused a sociocultural transition; the traditional nomadic lifestyle of the local people was gradually replaced by an agriculture-based population over the three decades [6], [7], [9].

Thus, the development of effective land-use practices, grassland management, and agricultural management technologies is crucial if the problems of land degradation and sandstorms in the Horqin Sandy Land are to be resolved.

V. CONCLUSION

Changes in land cover on the Horqin Sandy Land from 1975 to 2007 were identified and analyzed using Landsat images from 1975 (MSS), 1987 (TM), 1999 (ETM+), and 2007 (TM). ALOS and SPOT-5 images were used as supplementary data.

From a time series of remote sensing images, we determined the spatial distribution of nine land-cover classes and obtained information about temporal changes of land cover. We clearly demonstrated dramatic land-cover changes over the past three

decades in the Horqin Sandy Land region. During the rapid increase of human activities since 1975, the dominant changes were the conversion of grassland and woodland to cultivated land and shrinkage of areas covered by lakes and rivers. Our study showed that human activities have transformed a large proportion of natural landscapes into croplands over the period from 1975 to 2007. This has led to an increasing shortage of fresh water and to salinization problems on irrigated land. Development and implementation of sustainable regional land-use strategies that are suited to the fragile semi-arid region of the Horqin Sandy Land is urgently needed. Our study provides a baseline data set that can be used by researchers and policy makers to remediate the ongoing desertification of the Horqin Sandy Land and preserve the essential elements of the Mongolian culture of this region. Though outside the scope of this paper, the rainfall of that specific year probably has a influence on vegetation cover in this region. Further work needs to include satellite data with high temporal resolution (e.g., AVHRR and MODIS, etc.) to analyze the intra- and inter-annual variety of vegetation cover in this region.

REFERENCES

[1] T. Wang, W. Wu, H. Zhao, M. Hu, and A. Zhao, "Analyses on driving factors to sandy desertification process in Horqin Region, China," *J. Desert Res.*, vol. 24, no. 5, pp. 519–528, Sep. 2004, (in Chinese with English abstract).

[2] X. M. Wang, F. Chen, E. Hasi, and J. Li, "Desertification in China: An assessment," *Earth-Science Rev.*, vol. 88, no. 3–4, pp. 188–206, Jun. 2008.

[3] T. Takemi, "Explicit simulations of convective-scale transport of mineral dust in severe convective weather," *J. Meteorological Soc. Jpn. (Ser. II)*, vol. 83, no. A, pp. 187–203, Mar. 2005.

[4] Z. Decai and J. Qu, "Recent developmental trend and prediction of sand deserts in China," *J. Arid Environments*, vol. 53, no. 3, pp. 317–329, Mar. 2003.

[5] T. Wulan, D. Wu, and Y. Na, "The population change in Horqin in the 20th Century," *Acta Geographica Sinica*, vol. 62, no. 4, pp. 418–426, Apr. 2007.

[6] G. Jiang, X. Han, and J. Wu, "Restoration and management of the Inner Mongolia grassland require a sustainable strategy," *Ambio A J. Human Environment*, vol. 35, no. 5, pp. 269–270, Aug. 2006.

[7] S. Brogaard and X. Y. Zhao, "Rural reforms and changes in land management and attitudes: A case study from Inner Mongolia, China," *Ambio A J. Human Environment*, vol. 31, no. 3, pp. 219–225, May 2002.

[8] S. Brogaard and X. Li, "Agricultural performance on marginal land in Eastern Inner Mongolia, China—Development in the pre- and post-1978 reform periods," *Geojournal*, vol. 64, no. 3, pp. 163–175, Nov. 2005.

[9] H. Jiang, "Grassland management and views of nature in China since 1949: Regional policies and local changes in Uxin Ju, Inner Mongolia," *Geoforum*, vol. 36, no. 5, pp. 641–653, Sep. 2005.

[10] Wulantuya, "Land reclamation and land-use changes during last 50 years in Ke'erqin deserts, Inner Mongolia," *Progr. Geography*, vol. 19, no. 3, pp. 273–278, 2000, (in Chinese with English abstract).

[11] H. Tang, Y. Chen, and X. Li, "Driving mechanisms of desertification process in the Horqin Sandy Land—A case study in Zhalute Banner, Inner Mongolia of China," *Frontiers of Environmental Sci. Eng. China*, vol. 2, no. 4, pp. 487–493, Dec. 2008.

[12] Y. Gu, W. I. Rose, and G. J. S. Bluth, "Retrieval of mass and sizes of particles in sandstorms using two MODIS IR bands: A case study of April 7, 2001 sandstorm in China," *Geophysical Res. Lett.*, vol. 30, no. 15, p. 1805, Aug. 2003.

[13] Y. Bao, Wulantuya, Xiangbao, and X. Zhao, "Studies on the movement of farmland gravity and analyses of its driving forces in Inner Mongolia, China," *Progr. Geography*, vol. 17, no. 4, pp. 47–54, 1998, (in Chinese with English abstract).

[14] J. A. Foley, R. DeFries, G. P. Asner, C. Barford, G. Bonan, S. R. Carpenter, F. S. Chapin, M. T. Coe, G. C. Daily, H. K. Gibbs, J. H. Helkowski, T. Holloway, E. A. Howard, C. J. Kucharik, C. Monfreda, J. A. Patz, I. C. Prentice, N. Ramankutty, and P. K. Snyder, "Global consequences of land use," *Science*, vol. 309, no. 5734, pp. 570–574, Jul. 2005.

[15] D. Lu, P. Mausel, E. Brondizio, and E. Moran, "Change detection techniques," *Int. J. Remote Sens.*, vol. 25, no. 12, pp. 2365–2407, Jun. 2004.

[16] K. M. Bergen, T. Zhao, V. Kharuk, Y. Blam, D. G. Brown, L. K. Peterson, and N. Miller, "Changing regimes: Forested land cover dynamics in Central Siberia 1974 to 2001," *Photogramm. Eng. Remote Sens.*, vol. 74, no. 6, pp. 787–798, Jun. 2008.

[17] G. Chander, B. L. Markham, and D. L. Helder, "Summary of current radiometric calibration coefficients for Landsat MSS, TM, ETM+, and EO-1 ALI sensors," *Remote Sens. Environ.*, vol. 113, no. 5, pp. 893–903, May 2009.

[18] H. L. Zhao, R. L. Zhou, T. H. Zhang, and X. Y. Zhao, "Effects of desertification on soil and crop growth properties in Horqin Sandy cropland of Inner Mongolia, north China," *Soil & Tillage Res.*, vol. 87, no. 2, pp. 175–185, Jun. 2006.

[19] J. Liu, M. Liu, H. Tian, D. Zhuang, Z. Zhang, W. Zhang, X. Tang, and X. Deng, "Spatial and temporal patterns of China's cropland during 1990–2000: An analysis based on Landsat TM data," *Remote Sens. Environ.*, vol. 98, no. 4, pp. 442–456, Oct. 2005.

[20] LREIS Data, Resources and Environment Database of China (1:4,000,000), State Key Laboratory of Resources and Environment Information System, Institute of Geographic Sciences and Natural Resources Research, Chinese Academy of Sciences, Beijing (with CD-ROM), 1996.

[21] H. I. Reuter, A. Nelson, and A. Jarvis, "An evaluation of void-filling interpolation methods for SRTM data," *Int. J. Geographic Inform. Sci.*, vol. 21, no. 9, pp. 983–1008, Jan. 2007.

[22] K.-L. Du, "Clustering: A neural network approach," *Neural Networks*, vol. 23, no. 1, pp. 89–107, Jan. 2010.

[23] T. Kohonen, "Self-organized formation of topologically correct feature maps," *Biol. Cybern.*, vol. 43, no. 1, pp. 59–69, Jan. 1982.

[24] Z. Li and J. R. Eastman, "The nature of and classification of unlabelled neurons in the use of Kohonen's self-organizing map for supervised classification," *Trans. GIS*, vol. 10, no. 4, pp. 599–613, Jul. 2006.

[25] H. Bagan, Q. Wang, M. Watanabe, S. Karneyarna, and Y. Bao, "Land-cover classification using ASTER multi-band combinations based on wavelet fusion and SOM neural network," *Photogramm. Eng. Remote Sens.*, vol. 74, no. 3, pp. 333–342, Mar. 2008.

[26] E. Oja, *Subspace Methods of Pattern Recognition*. Letchworth, U.K.: Research Studies Press–Wiley., 1983.

[27] H. Bagan, Y. Yasuoka, T. Endo, X. Wang, and Z. Feng, "Classification of airborne hyperspectral data based on the average learning subspace method," *IEEE Geosci. Remote Sens. Lett.*, vol. 5, no. 3, pp. 368–372, Jul. 2008.

[28] S. Watanabe, P. F. Lambert, C. A. Kulikowski, J. L. Buxton, and R. Walker, "Evaluation and selection of variables in pattern recognition," in *Comput. Inform. Sci. II*. New York: Academic, 1967, pp. 91–122.

[29] J. Laaksonen and E. Oja, "Subspace dimension selection and averaged learning subspace method in handwritten digit classification," in *Proc. Int. Conf. Artificial Neural Networks*, Bochum, Germany, Jul. 16–19, 1996, pp. 227–232.

[30] H. Bagan, W. Takeuchi, Y. Yamagata, X. Wang, and Y. Yasuoka, "Extended averaged learning subspace method for hyperspectral data classification," *Sensors*, vol. 9, no. 6, pp. 4247–4270, Jun. 2009.

[31] R. G. Congalton and K. Green, *Assessing the Accuracy of Remotely Sensed Data: Principles and Practices*. Boca Raton, FL: Lewis Publishers, 1999, 137 p.

[32] L. Zhang, Z. Liu, R. Zhou, and S. Zhai, "Farmland expansion prediction at a pastoral village in northeastern China: A spatially explicit targeting approach," *Environmental Earth Sci.*, vol. 59, no. 4, pp. 847–852, Dec. 2009.

[33] L. Xun and Z. Bao, "Government, market and households in the ecological relocation process: A sociological analysis of ecological relocation in S banner," *Social Sci. China*, vol. 29, no. 1, pp. 113–128, Feb. 2008.

[34] X. Wang, T. Wang, Z. Dong, X. Liu, and G. Qian, "Nebkha development and its relationship to wind erosion and land degradation in semi-arid northern China," *J. Arid Environments*, vol. 65, no. 1, pp. 129–141, Apr. 2006.

Hasi Bagan received the B.S. degree in mathematics from Peking University, China, in 1991, the M.S. degree in mathematics from the Beijing University of Aeronautics and Astronautics, China, in 1996, and the Ph.D. degree from the Institute of Remote Sensing Applications, Chinese Academy of Sciences, China, in 2004.

From 2004 to 2006, he was a postdoctoral researcher with the National Institute for Environmental Studies, Japan. From 2006 to 2008, he was a JSPS Postdoctoral Fellow in the Institute of Industrial Science, University of Tokyo, Japan. He is currently a NIES Fellow with the National Institute for Environmental Studies, Japan. His research interests are land cover classification, neural network, wavelet fusion, and subspace algorithms.

Yuhai Bao received the B.S. degree in geographical science from Inner Mongolia Normal University, China, in 1989, the M.S. degree in physical geography from Northeast Normal University, China, in 1992, and the Ph.D. degree from the Institute of Remote Sensing Applications, Chinese Academy of Sciences (CAS) in 1999.

He is currently a Professor in the College of Geographical Science, Inner Mongolia Normal University. He is also an Associate Dean in the College of Geographical Science, Inner Mongolia Normal University, and Director of the Inner Mongolia Autonomous Region Key Laboratory for Remote Sensing and GIS. His research interests include land resources, desertification, natural calamities, eco-environment, soil erosion, geology, wetlands, and water resources assessment.

Wataru Takeuchi received the B.Eng., M.Eng., and Ph.D. degrees in civil engineering from the University of Tokyo, Tokyo, Japan, in 1999, 2001, and 2004, respectively.

He is currently an Assistant Professor at the Institute of Industrial Science, University of Tokyo. His research interests include agriculture remote sensing and image processing.

Yoshiki Yamagata received the B.S. degree in system science and the Ph.D. degree from the University of Tokyo, Tokyo, Japan, in 1985 and 1997.

He was a Researcher with the National Institute for Agro-Environmental Sciences, Japan from 1985 to 1991. In 1991, he joined the National Institute for Environmental Studies, Japan, and since then, he has been a Senior Researcher, Research Manager, and currently Special Senior Researcher in the Center for Global Environmental Research. His major research fields are remote sensing, geographic information system, and spatial data analysis for environment and disaster assessment.

Dr. Yamagata received the First Oze Prize in 1998, and the Best Paper Award from the Japan Simulation Society in 2006. He also serves as an editor of *Climate Policy*, *Environmental Science and Policy*, and *Applied Energy*.

Tsuguki Kinoshita received the B.Eng. degree, the M.Eng. degree in naval architecture, and the Dr.Eng. degree from the University of Tokyo, Tokyo, Japan, in 1993, 1996, and 1999, respectively.

He is currently an Associate Professor in the College of Agriculture, Ibaraki University, Japan. His research topic is global land-use modeling and woody biomass potential survey. He is a member of the Representative Concentration Pathways (RCPs) task team.